RSC Medicinal Chemistry

ROYAL SOCIETY OF CHEMISTRY

RESEARCH ARTICLE

View Article Online
View Journal | View Issue

Cite this: *RSC Med. Chem.*, 2025, **16**, 379

Ligand-centred phenotype-driven development of potent kinase inhibitors against oesophageal cancer†

Cecilia C. Ayala-Aguilera, [ab] Yang Ge, [ab] Álvaro Lorente-Macías, [ab] Benjamin N. Jones, [ab] Catherine Adam, [ab] Neil O. Carragher [ab] and Asier Unciti-Broceta [*ab]

Received 25th July 2024,
Accepted 13th October 2024

DOI: 10.1039/d4md00579a

rsc.li/medchem

Oesophageal cancer (OC) is one of the leading causes of cancer-related deaths worldwide. Due in part to its high heterogeneity, OC prognosis remains poor despite the introduction of targeted and immunotherapy drugs. Although numerous kinases play a significant role in the oncogenesis and progression of OC, targeting kinases have shown so far limited therapeutic success. Based on our understanding of the pharmacological properties of the pyrazolo[3,4-*d*]pyrimidine scaffold and the complex biology of OC, we implemented a ligand-centred strategy combined with phenotypic screening to develop novel antiproliferative inhibitors against OC. This approach is specifically designed to accelerate the discovery of lead compounds in cancers of high molecular heterogeneity such as OC. In an iterative process driven by structure–antiproliferative activity relationships (SAARs), we synthesised and tested 54 novel pyrazolo[3,4-*d*]pyrimidine derivatives against OC cell lines. The lead compound **2D7** (a.k.a. eCCA352) induces pan-OC activity and cell cycle arrest in the submicromolar range and was determined to inhibit Aurora kinase A, providing a new starting point to develop anticancer targeted agents against OC.

Introduction

According to the Global Cancer Observatory,[1] OC accounts for 3.1% of all cancer-related deaths, making it the sixth leading cause of cancer mortality globally. The two primary histological types are oesophageal squamous cell carcinoma (OSCC) and oesophageal adenocarcinoma (OAC).[2] Despite advancements in diagnosis and treatment, including the introduction of immunotherapy and targeted drugs against HER2 (trastuzumab) and TRK (entrectinib, larotrectinib), early-stage OC patients have a 5-year survival rate between 15% and 50%, while those with advanced disease face a survival rate of approximately one year.[3–5] One of the major issues in the treatment of OC patients is the high heterogeneity of this cancer, which is driven by large scale genomic rearrangements.[6] Consequently, there is not only an urgent medical need for improved therapies against OC, but also a demand to run drug discovery programmes that tackle the complexity of the disease.

Kinases play critical roles in both physiological and pathological cellular functions, including in the genesis and progression of malignancies, making them attractive targets for cancer therapy. In OC, several kinases are overexpressed and/or mutated including Aurora kinases,[7] enzymes that play a pivotal role in the cell cycle. Aurora kinase A (AURKA), in particular, is a Serine/Threonine kinase involved in mitotic cell division.[8] Cross-talk between AURKA and other pathways contributes to the development of various human cancers.[8,9] AURKA is a crucial regulatory constituent of the p53 pathway and promotes oncogenesis through several mechanisms including uncontrolled proliferation, increased cancer cell survival, inhibition of autophagy, aneuploidy and genetic instability.[10,11] AURKA overexpression and *AURKA* gene amplifications/mutations have been linked to resistance to cancer therapy, including resistance to chemotherapy, targeted and endocrine therapies, and radioresistance.[12–15] Importantly, overactivation of AURKA has been linked to OC malignancy,[14,16] is associated with tumour formation, proliferation and metastasis in both histological subtypes,[13,17] and has been proposed as a prognostic and therapeutic biomarker for OSCC.[15]

Pyrazolopyrimidines are nitrogen-containing heterocycles with high value in drug discovery consisting of the fusion of a pyrazole and a pyrimidine ring.[18,19] As bioisosteres of adenine, they can mimic key interactions of adenosine and ATP. Among their isomeric forms, the pyrazolo[3,4-*d*]

[a] *Edinburgh Cancer Research, Institute of Genetics & Cancer, University of Edinburgh, Crewe Road South, Edinburgh EH4 2XR, UK. E-mail: asier.ub@ed.ac.uk*
[b] *Cancer Research UK Scotland Centre, UK*

† Electronic supplementary information (ESI) available: Methods and characterisation of intermediates and final compounds, NMR spectra of lead compounds, biological protocols, Tables S1 and S2 and Fig. S1–S6. See DOI: https://doi.org/10.1039/d4md00579a

pyrimidine scaffold stands out for its diverse pharmacological profile, including herbicidal, antimicrobial, anti-inflammatory, cardiovascular, and anticancer activities.[20] The anticancer potential of pyrazolo[3,4-*d*]pyrimidines was first noted in 1956 with the discovery of 4-aminopyrazolo[3,4-*d*]pyrimidine. Later, PP1 and PP2 were identified as promiscuous SRC family kinase inhibitors. Since then, extensive research has led to several clinical approvals, including seven FDA-approved kinase inhibitors featuring pyrazolopyrimidine isomers. Ibrutinib was the first FDA-approved pyrazolo[3,4-*d*]pyrimidine derivative for leukaemia and lymphomas, targeting BTK kinase irreversibly. The second, umbralisib, is a dual PI3Kδ/CK1ε kinase inhibitor for lymphoma. Further development of pyrazolo[3,4-*d*]pyrimidine-containing kinase inhibitors continues to thrive through various medicinal chemistry strategies.[20] However, there have not yet been reports of pyrazolo[3,4-*d*]pyrimidine analogues with potent activity against OC models.[21,22]

Among over 80 clinically approved small molecule kinase inhibitors, only pan-TRK inhibitors larotrectinib and entrectinib (Fig. 1) are currently employed for the treatment of OC, specifically for a small subset of OSCC patients.[23,24] Larotrectinib, is a small-molecule TRK inhibitor used for the treatment of distinct types of cancers with *NTRK* gene fusion. *NTRK1* alterations in OSCC have been detected in rare cases. Therefore, larotrectinib can be considered as a therapeutic option for these patients. Entrectinib, another small-molecule TRK inhibitor, may also be used to treat *NTRK* fusion-positive OSCC.[5,25,26] Further studies are still required to determine the true efficacy of these targeted agents as first-line options to treat OSCC,[25,27] whereas the choice of targeted therapies for OAC patients is even lower. Due to the heterogeneity of OC, drug discovery approaches that incorporate phenotypic screening across genetically distinct human OC cell lines to develop kinase inhibitors with tailor-made pharmacodynamic profiles suited to treat this complex cancer could accelerate the discovery of novel treatments.

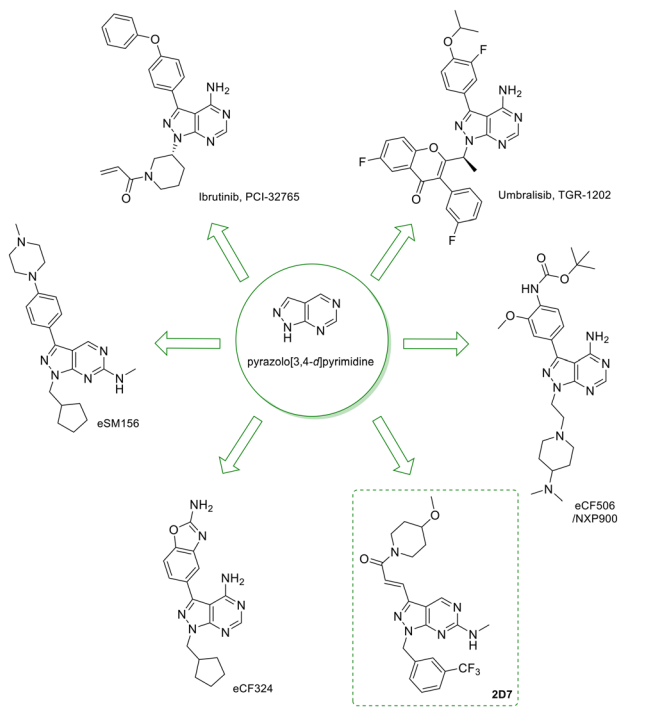

Fig. 1 Chemical structures of small-molecule kinase inhibitors containing the pyrazolo[3,4-*d*]pyrimidine scaffold. Clinically approved kinase inhibitors, ibrutinib and umbralisib, along with compounds from in-house studies: eSM156, eCF324, and eCF506/NXP900. The main lead compound discovered in this study, **2D7**, is also presented.

Our efforts to combine ligand-based design and phenotypic assays to speed up the identification of novel antiproliferative inhibitors based on the pyrazolo[3,4-*d*]pyrimidine scaffold has led to the discovery of potent kinase inhibitors, including the selective SRC/YES inhibitor eCF506 (a.k.a. NXP900, Fig. 1),[28,29] currently in phase 1. This strategy capitalises on the structural similarities of this heterocycle to adenine and its versatile proclivity to inhibit different kinase families, having produced inhibitors of PI3Ks and mTOR, or receptor tyrosine kinases such as AXL and FLT3.[30–33] More recently, eDB333 was discovered as a selective CSF-1R inhibitor.[34]

Herein, we present the application of this strategy towards the discovery of novel pyrazolo[3,4-*d*]pyrimidine derivatives with anti-OC properties, driven by phenotypic screening of OC cell lines, and the identification of their kinase targets by kinome screening.

Results and discussion

Design, synthesis and screening of libraries 1A and 2A

Fraser *et al.* explored the 4-aminopyrazolo[3,4-*d*]pyrimidine scaffold of PP1 and discovered eCF324, a dual PI3K/mTOR inhibitor, and eCF506, a potent and selective SRC family inhibitor (Fig. 1).[28,30] Later, Myers *et al.*, investigated the 6-methylaminopyrazolo[3,4-*d*]pyrimidine scaffold of UNC569 (ref. 35) to perform a target-biased drug discovery campaign that led to the discovery of eSM156, a potent FLT3 kinase inhibitor.[32] These and other representative works[35–38] have demonstrated that modifications of the N1 and C3 positions of the pyrazolo[3,4-*d*]pyrimidine scaffold have enormous influence on the kinome selectivity profile and potency of the resulting analogues.

In this work, we aimed to further explore the impact of the substituent at the C3 position of the pyrazolopyrimidine core by introducing an acryloyl bridge that allows amide-functionalisation using a range of primary and secondary amines. The acrylamide moiety is a versatile group in drug discovery, enabling from the formation of irreversible covalent bonds with the target protein (when the group is activated for Michael additions) to the establishment of multiple non-covalent H-bonding interactions (for deactivated acrylamides), being frequently present in approved drugs for the treatment of different disorders, including cancer.[24,39,40] In the present design, the acrylamide bridge is deactivated by the heterocyclic core and is introduced to restrict the conformational freedom of the C3 substituent and explore potential H-bonding interactions

between the amide group and the ATP-binding site of different kinases.

Two new compound libraries, **library 1A** and **library 2A**, containing an acrylamide moiety at the C3 position, were synthesised using the synthetic route described in Scheme 1. For **library 1A**, commercially-available 5-amino-1*H*-pyrazole-4-carbonitrile (**1**) was used to synthesise 1-(cyclopentylmethyl)-3-iodo-1*H*-pyrazolo-[3,4-*d*]pyrimidin-4-amine (**4**), as previously described.[28] The synthesis of **library 2A** started from 6-chloro-1*H*-pyrazolo[3,4-*d*]pyrimidine (**5**), which was used to synthesise 1-(cyclopentylmethyl)-3-iodo-*N*-methyl-1*H*-pyrazolo[3,4-*d*]pyrimidin-6-amine (**8**), as described by Myers *et al.*[32] The novel chemistry for the preparation of each library member comprised three synthetic steps. Palladium-catalysed Mizoroki–Heck cross-coupling with methyl acrylate worked efficiently and afforded the expected β-arylated products **9** (for **library 1**) and **11** (for **library 2**), in excellent yield. The ester group was then hydrolysed under basic conditions to afford the corresponding carboxylic acid intermediates **10** and **12**, respectively, in moderate yield. Finally, the carboxylic group of each of the intermediates was coupled with a set of commercially-available cyclic amines to yield the final compounds (**1A1–10** and **2A1–10**) in good overall yield (36–99%).

To obtain SAARs towards OC treatment, compounds **1A1–10** and **2A1–10** were tested against OE33 and FLO-1 cells, two representative models of OC. Inhibition of cell proliferation was used as the primary output and EC_{50} values were calculated using 9-point semi-logarithmic dose–response curves (0.003 to 30 μM). Paclitaxel (potent cytotoxic drug used in OC therapy)[41] and eCF506 were used as a positive control and kinase-inhibitor control, respectively. The corresponding ester and carboxylic acid intermediates were included in the screening. Fig. 2a shows the results of **library 1A**. Most tested compounds were inactive against both OE33 and FLO-1 cells. Only compound **1A6** and **1A10** showed marginal activity against FLO-1 with EC_{50} values close to 30 μM. These compounds have two different cyclic amine derivatives at the acrylamide moiety, providing poor SAARs.

Screening of **library 2A** generated more useful information (see Fig. 2b), with an overall increase in the antiproliferative potency of the compounds towards the FLO-1 cancer cell line in comparison to compounds **1A1–10**. The most potent compound from this library was **2A7**, with EC_{50} values lower than 9 μM against OE33 and FLO-1 cell lines. The methoxy group present in the "R" moiety of compound **2A7** suggests that a H-bond acceptor of low polarity at the para position of the piperidine is important for the activity of the derivative. In contrast, a nonpolar methyl group (**2A3**) or a polar H-bond donor group such as OH (**2A5**) did not favour cellular potency. The lack of activity of intermediates **10** and **12** confirmed the requirement of the cyclic amine moieties at the top of the molecule for antiproliferative activity. Of note, this screening showed the importance of the scaffold for

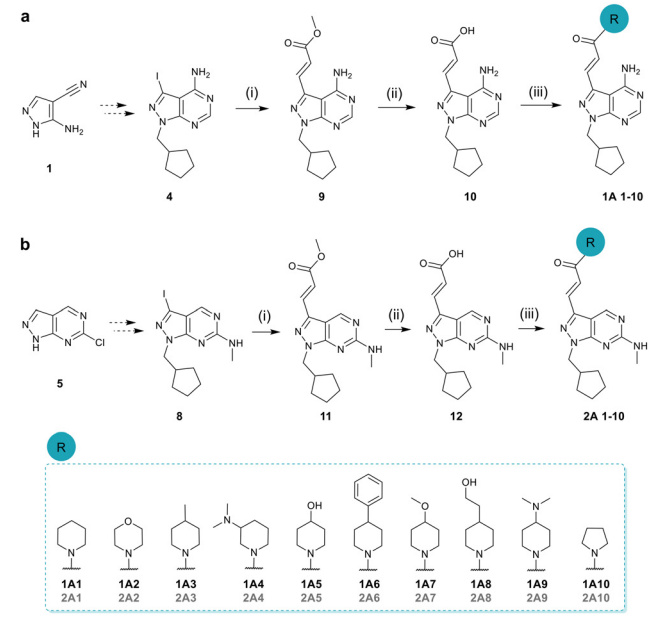

Scheme 1 Synthesis of (a) **1A1–10** and (b) **2A1–10**. Reagents and conditions: (i) methyl acrylate, $Pd(PPh_3)_2Cl_2$, TBAI, TEA/DMF/water, under N_2, 80 °C, 24 h, 51–73%; (ii) aqueous NaOH, THF, 60 °C, 24 h, 40–100%; (iii) amine derivatives (R), DIPEA, HATU, DMF, under N_2, r.t, 24 h, 36–99%.

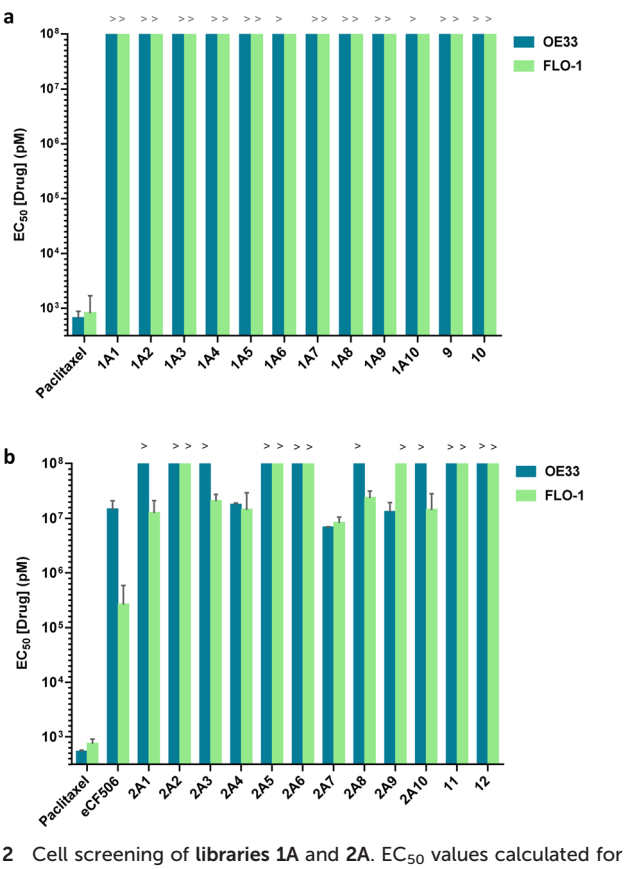

Fig. 2 Cell screening of **libraries 1A** and **2A**. EC_{50} values calculated for **1A1–10** (a) and **2A1–10** (b), intermediate compounds (**9–12**) and positive controls paclitaxel and eCF506 against OE33 and FLO-1 cells. Dose range: 0.003–30 μM. Cell viability was determined at day 5 using PrestoBlue reagent. Error bars: ±SD, n = 3.

activity: although compound **1A7** has the same 4-methoxypiperidine group at the C3-acrylamide moiety as **2A7**, the former is completely inactive. Results suggested that the 6-methylaminopyrazolo[3,4-*d*]pyrimidine scaffold could be more favourable to find potent antiproliferative leads against OC cells and therefore, **scaffold 2** was selected to progress the medchem programme.

Optimisation of N1. Design, synthesis, and screening of library 2B

SAARs from the initial libraries pointed to the enhanced potential of scaffold 2 and identified 4-methoxypiperidine as the best fragment to incorporate in the C3-acrylamide moiety. Based on this data, subsequent development was structured into three distinct stages: exploration of the N1 group, optimisation of the piperidine substituent at the C3-acrylamide group, and investigation of the alkyl group at the NH group of C6. First, **library 2B** was produced by replacing the original cyclopentylmethyl group at the N1-position with various alkyl groups, while maintaining the 4-methoxypiperidinyl moiety at the C3-acrylamide moiety unchanged. These structural alterations aimed to investigate their impact on antiproliferative effectiveness and to identify favourable combinations of substituents at the C3 and N1 positions. The synthetic pathway starts from common intermediate 7, which underwent alkylation reaction with various bromomethyl derivatives (instead of (iodomethyl) cyclopentane). The resulting intermediates were reacted with methyl acrylate, *via* Mizoroki–Heck reaction, followed by ester hydrolysis and 4-methoxypiperidine coupling (Scheme 2).

The antiproliferative properties of compound **library 2B** was tested against OE33 and FLO-1 cancer cell lines using Paclitaxel and eCF506, as positive controls. As shown in Fig. 3, compounds **2B10** and **2B11** demonstrated approximately three-fold greater potency compared to the reference compound **2A7**, while **2B8** and **2B9** showed similar EC_{50} values to **2A7**. The SAARs analysis uncovered key information about the impact of N1-substituents in scaffold 2. The introduction of oxygen atoms within the alkyl chains (**2B4–7**), and branched alkyl groups (**2B1–3**), had a negative effect on potency. Conversely, SAARs analysis revealed that the introduction of six-membered rings at the N1 position of the structure (**2B8–11**), especially benzene groups, enhanced antiproliferative activity. Compound **2B10**, with a methyl group at the *meta* position of the N1-benzyl substituent, exhibited the most potent antiproliferative activity, with EC_{50} values of 1.8 and 2.5 μM against OE33 and FLO-1, respectively. The importance of the *meta*-methyl group was confirmed by compound **2B11**, where replacing it with methoxy at the same position reduced potency.

Exploration of piperidine moiety. Design, synthesis, and screening of library 2C

Next, optimisation efforts were directed towards the piperidine group. A focused library was specifically designed

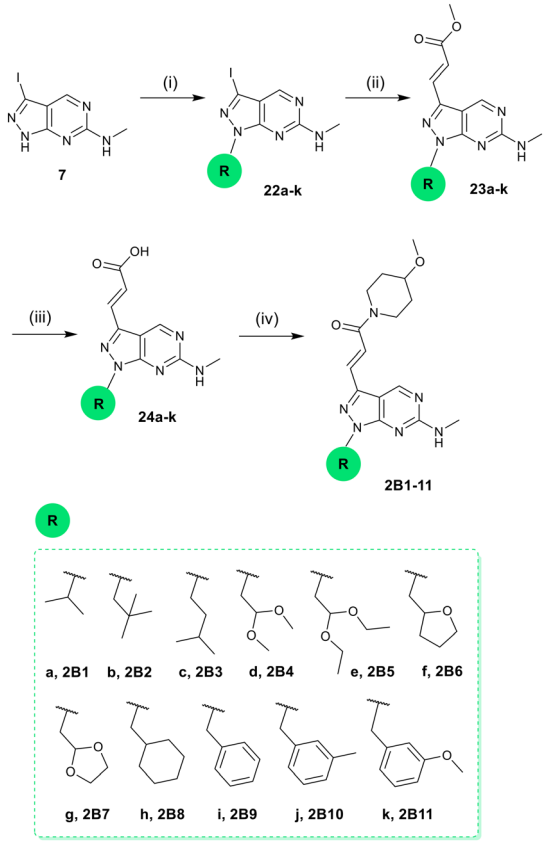

Scheme 2 Synthesis of **2B1–11**. Reagents and conditions: (i) alkyl bromide (R), NaH, DMF, 150 °C, μω, 85 min, 42–78%; (ii) methyl acrylate, $Pd(PPh_3)_2Cl_2$, TBAI, TEA/DMF/water, under N_2, 80 °C, 24 h, 45–99%; (iii) aqueous NaOH, THF, 60 °C, 24 h, 54–99%; (iv) 4-methoxypiperidine, DIPEA, HATU, DMF, under N_2 r.t, 24 h, 25–86%.

to investigate a small set of piperidine substituents at the C3-acrylamide moiety, while maintaining the *meta*-methylbenzyl at the N1 position. Four new compounds, **2C1–4**, were synthesized by reacting **24j** with 3-methoxypiperidine,

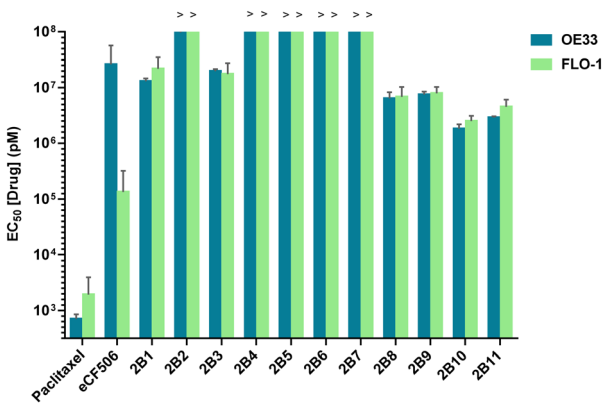

Fig. 3 Cell screening of **library 2B**. EC_{50} values calculated for **2B1–11** and positive controls paclitaxel and eCF506 against OE33 and FLO-1 cells. Dose range: 0.003–30 μM. Cell viability was determined at day 5 using PrestoBlue reagent. Error bars: ±SD, n = 3.

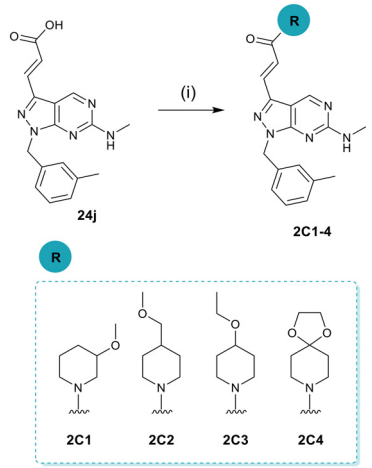

Scheme 3 Synthesis of **2C1–4**. Reagents and conditions: (i) substituted piperidine, DIPEA, HATU, DMF, under N_2, r.t, 24 h, 42–58%.

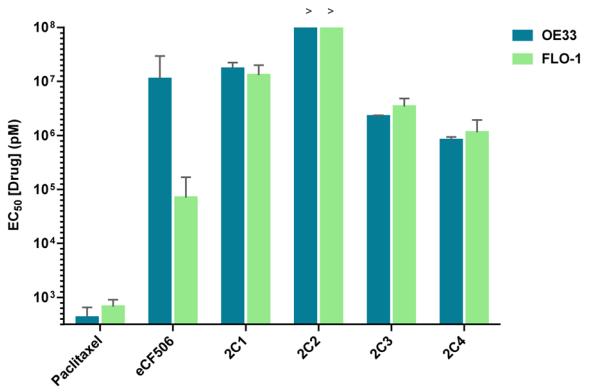

Fig. 4 Cell screening of **library 2C**. EC_{50} values calculated for **2C1–4** and positive controls paclitaxel and eCF506 against OE33 and FLO-1 cells. Dose range: 0.003–30 μM. Cell viability was determined at day 5 using PrestoBlue reagent. Error bars: ±SD, n = 3.

4-(methoxymethyl)piperidine, 4-ethoxypiperidine, and 1,4-dioxa-8-azaspiro[4.5]decane, respectively (Scheme 3).

As shown in Fig. 4, cell proliferation assays in OC cell lines indicated that modifications of the 4-methoxy group of the piperidine ring reduced potency, except for compound **2C4**, which incorporated 1,4-dioxa-8-azaspiro[4.5]decane (see dose response curves in ESI,† Fig. S1). Migration of the methoxy group at the 3-position of the piperidine (**2C1**) decreased the compound's activity, while substitution with a 4-methoxymethyl group (**2C2**) was even less tolerated. These results suggests that the position and size of the alkoxy moiety in the cyclic amine is critical for activity. Even compound **2C3**, which displays an ethoxy group instead of the methoxy of **2B10**, was significantly less potent. Notably, compound **2C4**, with two oxygens in a cyclic ketal group at the 4 position of the saturated ring, was the most potent of the series, with an EC_{50} of 0.83 μM against OE33 cells and 1.24 μM against FLO-1 cells, making it 2-fold more potent than **2B10**. Compound **2C4**, with an EC_{50} in the submicromolar range against OE33 cells, was considered the first antiproliferative lead compound of the project.

Benzyl group optimisation. Design, synthesis, and screening of library 2D

In the initial phase of investigation involving compound **2A7**, various alkyl groups were introduced at the N1 position. It was observed that the incorporation of six-membered rings significantly enhanced the anti-proliferative activity of compounds featuring a 4-methoxypiperidinyl group at the C3-acrylamide site. With this information in hand, the following optimisation work aimed to explore targeted modifications of the benzene ring at the N1 position. These alterations included repositioning the substituents within the benzyl group at N1 and introducing other hydrophobic substituents, such as the trifluoromethyl group. Concerned by the potential acid lability of the 1,4-dioxa-8-azaspiro[4.5] decane group, 4-methoxypiperidine was coupled to the C3-acrylic acid group.

Compound **library 2D** was prepared from common intermediate **7** by alkylation reaction with a selection of

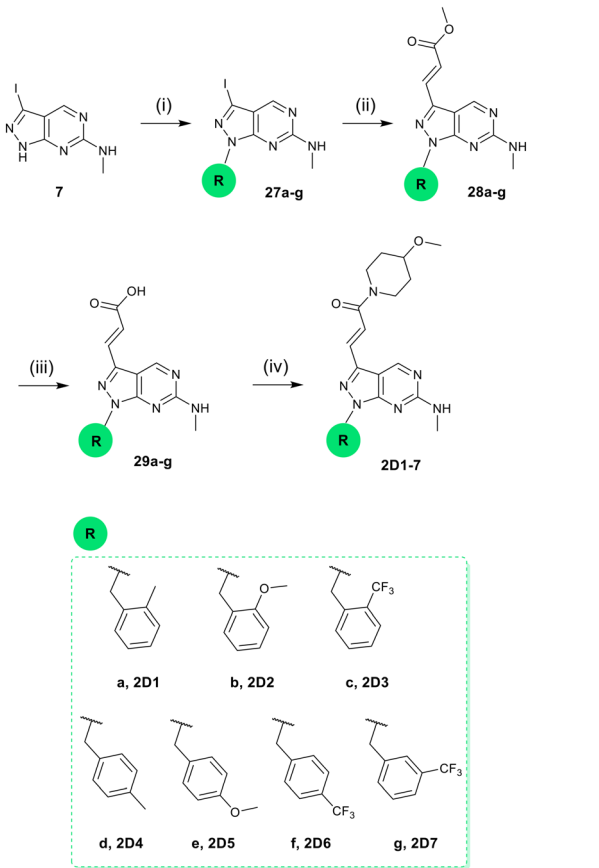

Scheme 4 Synthesis of **2D1–7**. Reagents and conditions: (i) benzyl bromide (R), NaH, DMF, 150 °C, μω, 85 min, 26–66%; (ii) methyl acrylate, $Pd(PPh_3)_2Cl_2$, TBAI, TEA/DMF/water, under N_2, 80 °C, 24 h, 18–82%; (iii) aqueous NaOH, THF, 60 °C, 24 h, 49–100%; (iv) 4-methoxypiperidine, DIPEA, HATU, DMF, under N_2 r.t, 24 h, 6–47%.

benzyl bromides to yield intermediates **27a–g** (Scheme 4). These intermediates were then subjected to a Mizoroki–Heck reaction with methyl acrylate, forming intermediates **28a–g**. Ester hydrolysis and amine coupling reactions with 4-methoxypiperidine led to the final compounds (**2D1–7**).

The cell proliferation screening against OE33 and FLO-1 cells (Fig. 5; see dose response curves in ESI,† Fig. S2) showed that the most potent compound of **library D** was **2D7**, containing a trifluoromethyl group at the *meta* position of the benzyl ring. Analysis of SAARs indicated that the positioning of substituents on the N1-benzyl group played a crucial role in maintaining high antiproliferative potency. The *meta* position was found to be the most favourable to incorporate hydrophobic groups (*e.g.*, methyl in **2B10**, or trifluoromethyl in **2D7**), while *ortho*-positioned substituents (**2D1**, **2D2** and **2D3**) led to a significant loss of potency. Interestingly, antiproliferative activity was partly restored exchanging the benzene substituents from *ortho* to *para* position (compounds **2D4**, **2D5** and **2D6**). Additionally, the lipophilic nature of the substituent also influenced antiproliferative potency. Compound **2D7**, which differed from **2B10** and **2B11** only in having a trifluoromethyl group instead of a methyl or methoxy group, exhibited a 7- and 13-fold increase in potency, respectively. With EC_{50} values of 0.24 and 0.36 μM against OE33 and FLO-1, respectively, compound **2D7** was the first compound to display submicromolar potency in both OC cell lines, being selected as the lead compound of the programme.

Exploration of the alkylamino group at C6. Design, synthesis, and screening of library 2E

The alkyl amino substituent at the C6 position is expected to have significant influence in the activity of pyrazolopyrimidines. As a last phase of the optimisation campaign, we investigated the introduction of a selection of amines at that position. **Library 2E** was prepared following the synthetic route described in Scheme 5. In brief,

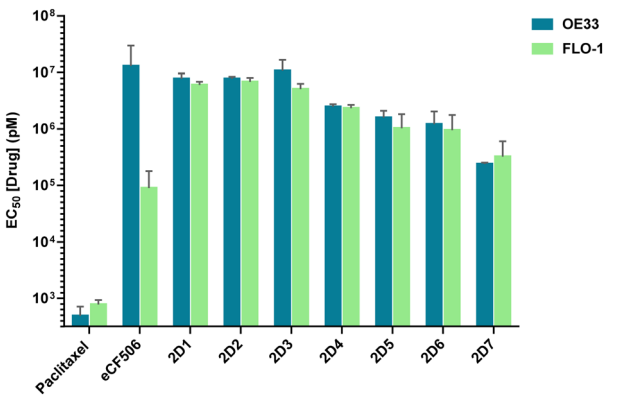

Fig. 5 Cell screening of **library 2D**. EC_{50} values calculated for **2D1–7** and positive controls paclitaxel and eCF506 against OE33 and FLO-1 cells. Dose range: 0.003–30 μM. Cell viability was determined at day 5 using PrestoBlue reagent. Error bars: ±SD, n = 3.

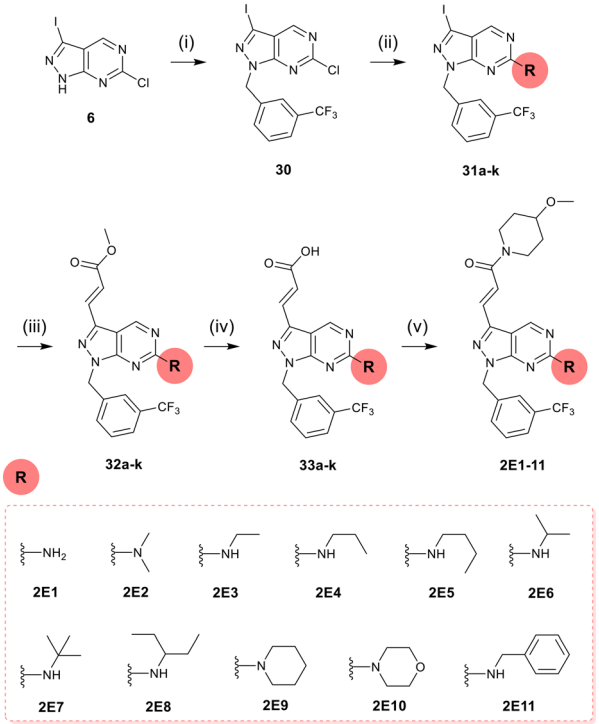

Scheme 5 Synthesis of **2E1–11**. Reagents and conditions: (i) 3-(trifluoromethyl)benzyl alcohol, DIAD, PPh_3, THF, under N_2, r.t, 50%; (ii) appropriate amine (R), THF, 150 °C, μω, 60 min; (iii) methyl acrylate, $Pd(OAc)_2$, PPh_3, TEA/dioxane, under N_2, 100 °C, 24 h, 79–97%; (iv) aqueous NaOH, THF, 60 °C, 24 h; (v) 4-methoxypiperidine, DIPEA, HATU, DMF, r.t, 2 h, 30–87%.

intermediate **6** was first alkylated with 3-trifluoromethylbenzyl bromide followed by SNAr with a selection of alkyl, dialkyl and cyclic amines. Palladium-catalysed Heck reaction of **31a–k** with methyl acrylate, ester hydrolysis and coupling with 4-methoxypiperidine led to the final compounds **2E1–11**.

To our surprise, screening of compounds **2E1** to **2E11** against OE33 and FLO-1 cells (Fig. S3 in ESI†) showed that none of the derivatives improved the antiproliferative properties of **2D7**. Analysis of SAARs showed the introduction of secondary amines led to inactive compounds, which indicates that a H-bond donor is required in that position. For monoalkylamines, the larger the alkyl group, the lower the activity of the analogue. The NH_2 derivative **2E1** did not improve the activity of **2D7** either, demonstrating that the optimal alkyl group for the position C6 of the scaffold is the original methylamino group.

Synthesis and screening of derivative 2F1

The most potent compounds yielded by the hit-to-lead optimisation campaign were **2C4** and **2D7**, both derived from hit compound **2B10** *via* different strategies. Compound **2C4** resulted from exploring modifications of the 4-position of the piperidine at the C3-acrylamide moiety, while **2D7** arose from N1-benzyl moiety optimisation. To combine the structural

features of both leads, hybrid compound **2F1** was synthesised with a 1,4-dioxa-8-azaspiro[4.5]decanyl group at the C3-acrylamide and 3-(trifluoromethyl)benzyl at the N1 position of the scaffold, as shown in Scheme 6.

Screening of compound **2F1** against OC cell lines found EC_{50} values of 0.56 μM against OE33 and 0.70 μM against FLO-1 (Fig. 6; see dose response curves in ESI,† Fig. S4), thus exhibiting higher antiproliferative efficacy than the hit compound **2C4**. However, it did not surpass the potency of compound **2D7**. While the hybrid compound did not exhibit the anticipated enhancement in antiproliferative efficacy, it still displayed submicromolar potency in both cell lines. Therefore, lead compounds **2F1** and **2D7**, along with **2C4**, were selected for a more comprehensive biological assessment.

Screening of lead compounds in additional OC models

Three potent antiproliferative compounds, **2C4**, **2D7** and **2F1**, were identified as leads for subsequent studies. To further assess their potential against the OAC histotype, the lead compounds were subjected to cell viability assay across an extended panel of heterogeneous OAC cell lines: MFD1, SKGT4, OAC-P4C and JH-EsoAd1. This broader panel was intended to evaluate the potential compounds' selectivity for specific OAC cell genotypes. Calculated EC_{50} values of the leads are plotted in Fig. 7. **2F1** exhibited strong antiproliferative activity against the entire extended cell panel. Its potency was slightly superior than that of **2D7** in three out of four cell lines, highlighting MDF-1 cells for which EC_{50} values were 0.92 for **2F1** and 2.57 μM for **2D7**. In contrast, **2D7** was more potent than **2F1** against SK-GT-4 (0.79 and 2.90 μM, respectively). When comparing **2C4** and **2F1**, the two leads displaying a 1,4-dioxa-8-azaspiro[4.5] decanyl group at the acrylamide moiety, **2F1** was in the range of 2-fold more potent in antiproliferative activity compared to **2C4**. This trend was consistent with the results obtained in OE33 and FLO-1 cells, suggesting that modifications in the N1-benzyl moiety of the compounds have a greater impact on potency than modifications in the C3-acrylamide moiety.

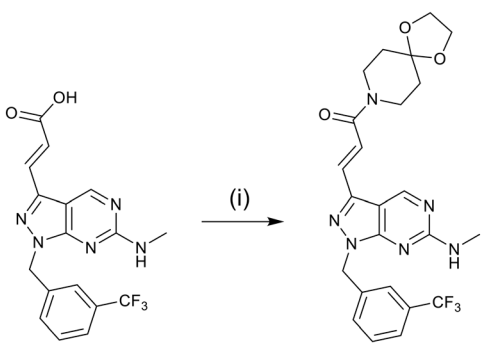

Scheme 6 Synthesis of **2F1**. Reagents and conditions: (i) 4-piperidone ethylene acetal, DIPEA, HATU, DMF, under N_2, r.t, 24 h, 56%.

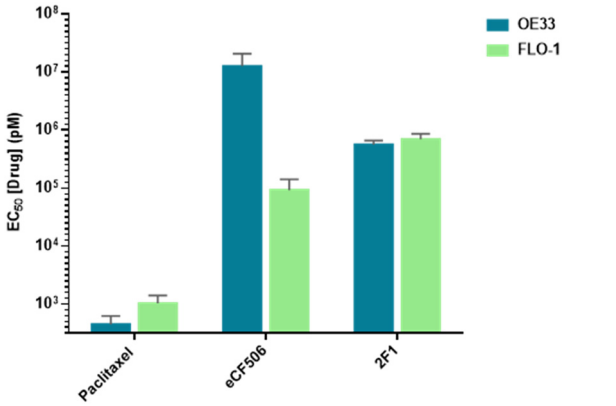

Fig. 6 Cell screening of compound **2F1**. EC_{50} values calculated for **2E1** and positive controls paclitaxel and eCF506 against OE33 and FLO-1 cells. Dose range: 0.003–30 μM. Cell viability was determined at day 5 using PrestoBlue reagent. Error bars: ±SD, n = 3.

The three compounds were then tested in two non-transformed human oesophageal cell models, including the pre-malignant CP-A, a cell line derived from Barrett's oesophagus tissue lesions,[42] and EPC-2, a normal oesophageal keratinocyte cell line immortalised with telomerase[43] (see Fig. S5 in ESI†). **2F1** was the compound that displayed greater potency against these pre-malignant cell lines. Although these cell models are immortalised and therefore highly proliferative, in contrast to the OC cell lines, these cell lines are both wild-type for the tumour suppressor gene p53. Therefore, most promising lead compounds should ideally demonstrate higher potency against OC cells originated from cancer patients. Based on the overall assessment of the antiproliferative properties of the lead compounds both in malignant and pre-malignant OC cells, **2D7** was selected as the lead for further biological evaluation.

Study of cell cycle arrest

Once **2D7** was chosen as the lead compound, we next studied its effects on the cell cycle. Cells were seeded at high densities (200 000 and 350 000 cells per well for OE33 and

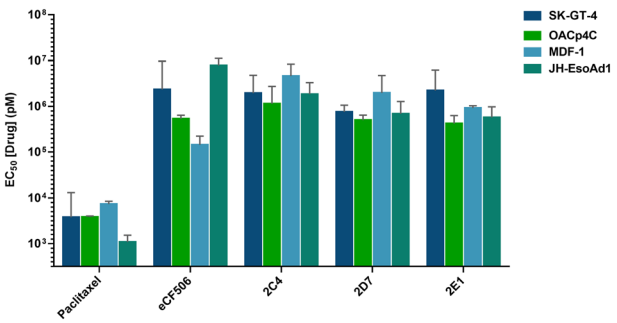

Fig. 7 Cell screening of lead compounds. EC_{50} values calculated for **2C4**, **2D7**, **2F1** and positive controls paclitaxel and eCF506 against SK-GT-4, OACp4C, MDF-1 and JH-EsoAd1 cells. Dose range: 0.003–30 μM. Cell viability was determined at day 5 using PrestoBlue reagent. Error bars: ±SD, n = 3.

FLO-1, respectively) and incubated for 48 h before treatment with 3 μM of lead compound **2D7**, employing 0.1% DMSO as a negative control. After 72 h incubation at standard cell culture conditions, the cells were fixed, stained for DNA, and analysed using flow cytometry.

Based on their DNA content, cells were distributed into G0/G1, S, G2/M, and sub-G1 phases. As shown in Fig. 8 (see full histograms in ESI,† Fig. S6), cell cycle analysis of the OE33 and FLO-1 cell lines treated with **2D7** indicated that the compound induces substantial alterations in the cell cycle of both cell types. Specifically, in OE33 cells, **2D7** prompted a rapid arrest of cells in the G2/M phase, indicating a suppression of cell growth leading to significant accumulation of cells in this phase, while reducing the G0/G1 phase. Additionally, the results suggested that the lead compound induced apoptosis, as evidenced by a slight increase in the number of cells in the sub-G1 phase in OE33 cells compared to the DMSO control.

In FLO-1 cells, treatment with the lead compound also led to significant perturbations in the cell cycle, but the effects differed from those observed in OE33 cells (Fig. 8). Treating FLO-1 cells with **2D7** resulted in an enrichment of cells in the S and G2/M phases, accompanied by a significant reduction in the G0/G1 phase relative to the DMSO control. These findings highlight the impact of the lead compound on cell cycle regulation, emphasising their potential in the context of OC therapy.

Target identification study: kinase profiling

The kinase inhibition properties of lead compound **2D7** was profiled against 340 protein kinases. The lead compound was screened at a single dose of 1 μM, in duplicate (assay performed by Reaction Biology). The kinome profiling results are reported as the mean percentage of enzymatic inhibition activity upon compound treatment compared to the untreated control. For clarity, Fig. 9 displays the kinome phylogenetic tree showing the selectivity of compound and a Table with the inhibition levels for selected kinases broadly associated with cancer. Complete results are available in the ESI† (Table S2).

As shown in Fig. 9a, lead compound **2D7** exhibited >50% inhibition against Aurora kinase A (AURKA). Other kinases such as LRRK2 were inhibited at lower levels. It is worth noting that **2D7** showed minimal to no inhibition of AXL, FLT3, and RET, which were the primary targets of eSM156, compound that inspired the use of scaffold 2. By inhibiting more potently one kinase isoform within the Aurora family, lead compound **2D7** demonstrates an interesting selectivity profile that may be associated to the molecular biology of

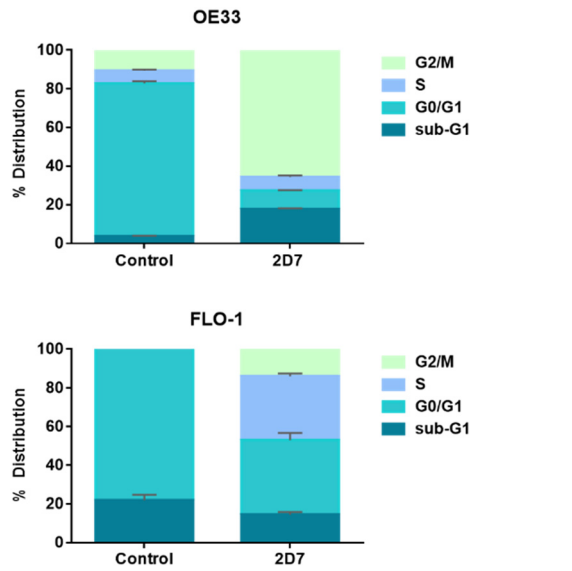

Fig. 8 Cell cycle study. The graphs depict the effects of **2D7** on the cell cycle of OE33 and FLO-1 cells, showing the distribution percentage (%) of each phase of the cell cycle. Cells were treated with **2D7** at 3 μM for 72 h, then stained with propidium iodide and analysed by flow cytometry. Error bars: ±SD, n = 2.

a

Kinase Name	% Inhibition [1uM]	Kinase Name	% Inhibition [1uM]
ABL1	7.74	TRKA	30.66
AuroraA	66.57	TRKB	24.46
AuroraB	19.19	TRKC	17.25
AuroraC	19.00	FLT3	13.36
BLK	15.91	JAK1	0.00
BRK	4.24	JAK2	0.99
BRSK1	3.57	JAK3	7.28
BUB1B	4.38	KIT	17.86
CDK1/CycA2	14.19	LRRK2	42.21
CDK4/CycD1	3.94	MET	8.85
CDK6/CycD1	14.15	MTOR	4.42
EGFR	0.00	PLK1	0.00
ERBB2	9.79	RET	13.20
FGFR1	9.63	VEGFR1	5.06
SYK	0.00	VEGFR2	6.94
SRC	0.98	VEGFR3	1.69

b

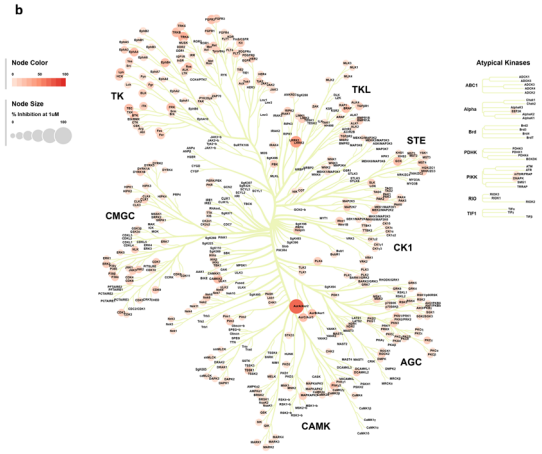

Fig. 9 Kinase inhibition profile of lead **2D7**. a) Summary of kinase profiling. Table shows the percentage of enzymatic inhibition after treatment with 1 μM of **2D7**, the mean percentage are respect to DMSO control. Colour scale highlights the inhibition percentage values from the lowest (green) to the highest (red). b) Kinome phylogenetic tree showing the selectivity of compound **2D7** for the Aurora kinase A over a panel 340 protein kinases. Note that only kinases listed on Coral software[44] were used for this plot. The size of the dots is relative to the mean percentage (%) of inhibition to the corresponding kinase at a dose of 1 μM. Where dots are not present, the kinase was not evaluated.

OC. Also, the results of the kinome profiling align with the mechanism through which lead compound **2D7** exerts its antiproliferative effects, as AURKA is a crucial regulatory protein governing different phases of the cell cycle, including G2/M transition.[7,8] In the context of OC, overexpression of AURKA has been associated with the malignancy and progression of this specific cancer type.[16,17,45–47] Nine-point semilog dose–response screening of **2D7** against recombinant AURKA (0.001 to 30 μM) provided an IC_{50} value of 1.45 μM (Fig. 10a). To further confirm direct target engagement, we performed a NanoBRET assay (outsourced to Reaction Biology).[48] HEK293 were transfected with Nano-Luc-Aurora A (fusion vector) and treated with **2D7** at a range of concentrations for 1 h. Luminescence measurements confirmed the direct dose-dependent binding of the lead compound to its target inside cells (see Fig. S7, ESI†).

Molecular docking of lead compound 2D7

Following the results from kinase profiling, an in-silico docking analysis was conducted to gain insights into the mode of binding of **2D7** to its kinase target (Fig. 10b). The available crystal structure was 1MQ4, representing the crystal structure of AURKA in complex with ADP.[49] The minimised energy 3D conformation of **2D7** was generated by DataWarrior,[50] and the optimised structure was independently docked into the kinase domain of the protein using AutoDock Vina[51] and visualised by PyMOL.[52]

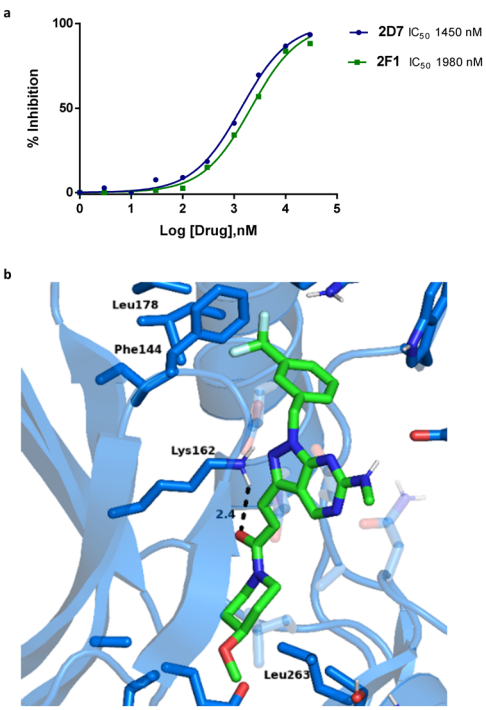

Fig. 10 (a) Dose response curves and calculated IC_{50} values of the inhibition of AURKA by **2D7** and **2F1**. (b) *In silico* docking of lead compound **2D7** in Aurora kinase A (PDB: 1MQ4). Key H bond interactions and their distances (Å) are shown as black dashes. Image was created using PyMOL.

The outcomes of the docking indicate that lead compound **2D7** is predicted to form direct interactions with the amino acids within the ATP-binding pockets of Aurora kinase A. The study predicts that **2D7** forms a H bond to the Lys162 residue of the β sheet, the atoms involved in this interaction are the oxygen atom of the acrylamide moiety of **2D7** and the backbone NH group of Lys162 (Fig. 10a). The trifluoromethyl group of the benzyl ring occupies an ATP binding site cleft formed by several lipophilic residues, including Phe144, Leu164, Leu169 and Leu178, whilst the 4-methoxy piperidine rings sit in the ATP-binding pocket, close to where the ADP was bound in the crystal structure. The residues present in the reported ATP-pocket are Leu210, Tyr212, Ala213, Leu139, Val147 and Leu 263.[49] These results are consistent with those of the kinase profiling that identified lead **2D7** as an AURKA inhibitor. Additional docking analyses performed for compounds **2C4**, **2F1** and closely related analogues of **2D7** are found in the ESI† (Fig. S8).

Finally, *in silico* analysis of the physicochemical and ADME properties of **2D7** (see Table S4, ESI†) suggests that this lead compound possesses promising properties for further lead optimisation.

Conclusions

The above medicinal chemistry campaign aimed to address the pressing need for improved treatments for OC, a disease associated with increasing incidence and high mortality rates worldwide. Capitalising on the chameleonic pharmacological properties of the pyrazolo[3,4-*d*]pyrimidine scaffold, whose substituents at N1, C3, C4 and C6 are known to drive the scaffold's inhibitory properties to various different kinase families, we performed a ligand-centred phenotypic screening strategy. After several iterations of design, synthesis and screening of compound libraries, we identified lead compounds with promising anti-cancer properties. Two potent lead compounds, **2D7** and **2F1**, demonstrated remarkable antiproliferative activity against OC cell lines. Further biological evaluation revealed that lead compound **2D7** induced significant alterations in the cell cycle, inducing cell growth arrest in OC cell lines. Moreover, kinase profiling studies unveiled its potential mechanism of action, showing that lead compound **2D7** (a.k.a. eCCA352) inhibited Aurora kinase A, which has a critical role in the regulation of cell cycle progression and signalling pathways implicated in OC development. This investigation further indicates that this kinase target may be relevant in OC and represents a promising starting point for further medchem work towards OC therapeutics.

Experimental section

Synthetic procedures

General methods: Chemicals and reagents commercially available were purchased from Acros Organics, Alfa Aesar, Fisher Scientific, Fluorochem, Sigma Aldrich and VWR

International. The reactions were performed in a Biotage® Initiator Third Generation microwave synthesiser or on a heating magnetic stirrer with temperature sensor. Flash column chromatography was performed with silica gel (220–440 mesh). NMR spectra were obtained at 300 K on 500 MHz, 400 MHz or 600 MHz Bruker spectrometers, and referenced relative to the solvent residual peaks with chemical shifts (δ) reported in ppm. Multiplicity is reported, as follows; chemical shift, integration, multiplicity (s = singlet, d = doublet, t = triplet, q = quartet and m = multiplet) and coupling constant (in Hz). LRMS were obtained using an Agilent 1260 Infinity II HPLC system. HRMS were obtained using a Bruker 12 T SolariX FT-ICR-MS spectrometer under electrospray ionisation conditions.

Synthesis of lead compound 2D7

6-Chloro-3-iodo-1*H*-pyrazolo[3,4-*d*]pyrimidine (6). 6-Chloro-1*H*-pyrazolo[3,4-*d*]pyrimidine (**5**) (1 g, 6.5 mmol) was suspended in DMF (14 ml). To this, *N*-iodosuccinimide (1.8 g, 7.8 mmol, 1.2 equiv.) was added. The reaction was heated at 120 °C using microwave radiation for 60 min. The reaction mixture was partitioned between water and EtOAc. The organic layers were combined and washed with water and brine, dried over anhydrous $MgSO_4$, and concentrated under vacuum. The crude product was purified by silica gel flash chromatography using MeOH/DCM (0–2%) to afford the desired product (853 mg, 3 mmol, 47%). ^{1}H NMR (500 MHz, DMSO-d_6) δ 14.64 (s, 1H), 9.02 (s, 1H). ^{13}C NMR (126 MHz, DMSO) δ 157.8 (C), 155.8 (CH), 155.2 (C), 117.6 (C), 94.16. LRMS (*m*/*z*) $[M + H]^+$: 281.00.

3-Iodo-*N*-methyl-1*H*-pyrazolo[3,4-*d*]pyrimidin-6-amine (7). 6-Chloro-3-iodo-1*H*-pyrazolo[3,4-*d*]pyrimidine (**6**) (500 mg, 1.78 mmol) was dissolved in THF (3 mL). Methylamine 2 N in THF (12 mL) was added and then the mixture was heated at 150 °C using microwave radiation for 60 min. The precipitate was dried by vacuum filtration and washed with water, no further purification was performed (302.5 mg, 1.2 mmol, 62%). ^{1}H NMR (500 MHz, DMSO-d_6) δ = 13.28 (s, 1H), 8.45 (s, 1H), 7.53 (s, 1H), 2.82 (d, J = 4.6, 3H). ^{13}C NMR (126 MHz, DMSO) δ 162.7 (C), 157.4 (C), 156.8 (CH), 153.9 (C), 93.3 (C), 28.4 (CH_3).

3-Iodo-*N*-methyl-1-{[3-(trifluoromethyl)phenyl]methyl}-1*H*-pyrazolo[3,4-*d*]pyrimidin-6-amine (27g). 3-Iodo-*N*-methyl-1*H*-pyrazolo[3,4-*d*]pyrimidin-6-amine (**7**) (113 mg, 0.410 mmol, 1 equiv.) was suspended in DMF (3.5 mL), and sodium hydride was added (20.4 mg, 0.509 mmol, 1.4 equiv., 60% dispersion in mineral oil), and the mixture stirred until gas evolution subsided. To this 3-(trifluoromethyl)benzyl bromide (0.546 mmol, 1.5 equiv.) was added, and the mixture was heated at 150 °C using microwave irradiation for 85 min. The mixture was partitioned between EtOAc and water, and the organic layers separated. The combined organic layers were washed with brine, dried over $MgSO_4$, and concentrated under vacuum. The crude product was purified by silica gel flash chromatography EtOAc/hexane (0–40%) to obtain the pure product (53.6 mg, 0.124 mmol, 30%). ^{1}H NMR (500 MHz, DMSO-d_6) δ = 8.47 (s, 1H), 7.78–7.71 (m, 2H), 7.67 (d, J = 7.7, 1H), 7.59–7.51 (m, 2H), 5.51 (s, 2H), 2.87 (d, J = 4.6, 3H). ^{13}C NMR (126 MHz, DMSO) δ 162.2 (C), 155.4 (C), 154.0 (C), 138.3 (CH), 132.0 (CH), 129.8 (CH), 129.06 (q, J C, F = 31.5, C), 124.7 (CH), 124.5 (CH), 124.05 (q, J C, F = 272.4, C), 111.7 (C), 93.2 (C), 48.9 (CH_2), 28.9 (CH_3).

Methyl(2*E*)-3-[6-(methylamino)-1-{[3-(trifluoromethyl)phenyl]methyl}-1*H*-pyrazolo[3,4-*d*]pyrimidin-3-yl]prop-2-enoate (28g). 3-Iodo-*N*-methyl-1-{[3-(trifluoromethyl)phenyl]methyl}-1*H*-pyrazolo[3,4-*d*]pyrimidin-6-amine (**27g**) (53.6 mg, 0.124 mmol, 1 equiv.) was dissolved in DMF/water/TEA (7.8 mL/0.78 mL/0.78 mL). To this, TBAI (2 equiv.), methyl acrylate (10 equiv.) and $Pd(PPh_3)_2Cl_2$ (0.2 equiv.) were added. The reaction vial was flushed with N_2 for 10 minutes and then heated at 80 °C using a heating magnetic stirrer for 24 hours. After cooling to r.t, the mixture was extracted with DCM. The combined organic layers were washed with brine, dried over $MgSO_4$, filtered through a plug of Celite® and concentrated under vacuum. The crude product was purified by silica gel flash chromatography using EtOAc/hexane (0–40%) to afford the desired product (29.5 mg, 0.075 mmol, 61%). ^{1}H NMR (500 MHz, chloroform-d) δ = 8.84 (s, 1H), 7.74 (d, J = 16.3, 1H), 7.71 (s, 1H), 7.57 (t, J = 9.0, 2H), 7.47 (t, J = 7.8, 1H), 6.96 (s, 1H), 6.63 (d, J = 16.3, 1H), 5.52 (s, 2H), 3.84 (s, 3H), 3.11 (d, J = 4.8, 3H). ^{13}C NMR (126 MHz, $CDCl_3$) δ 166.7 (C), 159.3 (C), 156.3 (C), 149.7 (CH), 142.3 (C), 136.6 (C), 134.7 (CH), 131.9 (CH), 131.3 (q, JC, F = 32.5, C), 129.5 (CH), 125.5 (CH), 125.3 (q, JC, F = 3.8, CH), 124.0 (q, JC, F = 272.4, C), 122.5 (CH), 106.3 (C), 52.2 (CH_3), 50.3 (CH_2), 28.5 (CH_3).

(2*E*)-3-[6-(Methylamino)-1-{[3-(trifluoromethyl)phenyl]methyl}-1*H*-pyrazolo[3,4-*d*]pyrimidin-3-yl]prop-2-enoic acid (29g). Methyl (2*E*)-3-[6-(methylamino)-1-{[3-(trifluoromethyl)phenyl]methyl}-1*H*-pyrazolo[3,4-*d*]pyrimidin-3-yl]prop-2-enoate (**28g**) (26.4 mg, 0.067 mmol, 1 equiv.) was suspended in THF (10 mL) and 6 M NaOHaq solution (10 equiv.) was added. The reaction was heated at 60 °C using a heating magnetic stirrer for 24 hours. Then, the solvent was evaporated under vacuum; the residue obtained was dissolved in water/EtOAc (1 : 1) and acidified (pH 4) with 1 M HCl. The product was extracted with EtOAc, the combined organic layers were dried under vacuum, and the product was allowed to dry in an oven at 40 °C overnight. The resulting product (31 mg, 0.082 mmol, 100%) was used without further purification. ^{1}H NMR (500 MHz, methanol-d_4) δ = 9.06 (s, 1H), 7.73 (d, J = 9.5, 1H), 7.68 (s, 1H), 7.60 (dt, J = 5.4, 3.0, 2H), 7.53 (t, J = 7.7, 1H), 6.74 (d, J = 16.3, 1H), 5.58 (s, 2H), 3.03 (s, 3H). ^{13}C NMR (126 MHz, MeOD) δ 169.5 (C), 161.6 (C), 157.7 (C), 153.2 (CH), 143.4 (C), 139.0 (C), 135.7 (CH), 133.0 (CH), 130.6 (CH), 132.0 (q, J C, F = 32.1, C), 125.8 (q, J C, F = 3.9, CH),125.49 (q, J C, F = 271.3, C),126.1 (CH), 124.1 (CH), 107.1 (C), 50.8 (CH2), 28.5 (CH_3).

(2*E*)-1-(4-Methoxypiperidin-1-yl)-3-[6-(methylamino)-1-{[3-(trifluoromethyl)phenyl]methyl}-1*H*-pyrazolo[3,4-*d*]pyrimidin-3-yl]prop-2-en-1-one (2D7). (2*E*)-3-[6-(Methylamino)-1-{[3-(trifluoromethyl)phenyl]methyl}-1*H*-pyrazolo[3,4-*d*]pyrimidin-3-yl]prop-2-enoic acid (**29g**) (31 mg, 0.082 mmol, 1 equiv.) was

dissolved in anhydrous DMF (4 mL). To this 4-methoxypiperidine (0.041 mL, 0.328 mmol, 4 equiv.) and DIPEA (0.043 mL, 0.243 mmol, 3 equiv.) were then added. The resulting mixture was stirred for 5 min before adding HATU (37.42 mg, 0.098 mmol, 1.2 equiv.). The reaction vial was flushed with N_2, and the reaction stirred at r.t for 24 hours. The solvent was removed under vacuum and the residue partitioned between water and EtOAc. The combined organic layers were washed with brine, dried over $MgSO_4$, and concentrated under vacuum. The crude product was purified by silica gel TLC plate using MeOH/DCM (5%); then using MeOH/DCM (8%) to afford the desired product (13.1 mg, 0.028 mmol, 34%). ^{1}H NMR (500 MHz, DMSO-d_6) δ = 9.24 (s, 1H), 7.76 (s, 1H), 7.68–7.64 (m, 2H), 7.58 (t, J = 7.5, 2H), 7.46 (d, J = 15.7, 1H), 7.35 (d, J = 15.8, 1H), 5.55 (s, 2H), 3.92 (dd, J = 13.9, 6.4, 2H), 3.43 (tt, J = 7.9, 3.7, 2H), 3.27 (s, 3H), 3.24 (d, J = 5.7, 1H), 2.87 (dq, J = 8.8, 3.4, 3.0, 3H), 1.84 (d, J = 15.2, 2H), 1.41 (ddd, J = 30.4, 15.2, 6.3, 2H). ^{13}C NMR (126 MHz, DMSO) δ 163.9 (C), 161.6 (C), 155.9 (C), 154.4 (CH), 141.5 (C), 138.2 (C), 132.0 (CH), 129.8 (CH), 129.19 (q, J C, F = 31.8 Hz, C) 124.6 (CH), 124.4 (CH), 124.4 (CH), 124.04 (q, J C, F = 272.3 Hz, C) 121.8 (CH), 104.8 (C), 75.0 (CH), 55.0 (CH3), 48.8 (CH_2), 43.9 (2 × CH_2), 31.4 (2 × CH_2), 27.7 (CH_3). HRMS (ESI, m/z) calcd for $C_{22}H_{26}F_3N_6O_2$ $[M + H]^+$: 475.2064; found, 475.2079.

Biological studies

The OC cell lines were purchased from the European Collection of Authenticated Cell Cultures (ECACC). General methods: FLO-1 and OE33 were cultured in RPMI (Gibco), supplemented with 10% (v/v) FBS (Gibco) and 2 mM L-glutamine (Gibco) in a standard incubator (95% humidity, 5% CO_2), and sub-cultured twice per week using trypsinisation. ESI† contain further information about the other cancer cell lines used in this work.

Dose–response cell viability assay

Cells (1 × 10^3 FLO-1 cells per well, 5 × 10^2 OE33 cells per well) were plated in 96-well plates in 100 μL of RPMI medium supplemented with 10% FBS and 2 mM L-glutamine and incubated for 48 h in an incubator at 37 °C and 5% CO_2. After 48 h, the media was aspirated and replaced with 95 μL of fresh medium. Stocks of the test compounds were prepared in DMSO at 100 mM. Serial dilution plates were then made with concentrations ranging from 30 mM to 3 μM. On the treatment day, intermediate dilution plates were prepared by diluting these serial dilutions 1 : 50 into the medium. Cells were treated with 5 μL from the intermediate dilution plates, resulting in final concentrations of 0.003–30 μM and a final DMSO concentration of 0.1% v/v. Untreated cells were incubated with DMSO (0.1% v/v). After 5 d, PrestoBlue cell viability reagent (10 μL) was added to each well, and the plates incubated for 90 min. Fluorescence emission was detected using an Envision fluorescence plate reader (excitation 550 nm, emission 580 nm). All conditions were normalised to the untreated cells (100%), and curves were fitted using a four-parameter logistic fit with minimum value constrained to zero using GraphPad Prism software, to calculate EC_{50} values.

Cell cycle assay

OE33 and FLO-1 cells were seeded in 6-well plates at 200 000 and 350 000 cells per well, respectively, and incubated for 48 hours. The medium was then replaced with fresh medium containing 3 μM of the tested compounds or DMSO (0.1% v/v). After a further 72-hour incubation at 37 °C, the medium from OE33 cells was discarded, while the medium from FLO-1 cells was collected. Cells were trypsinised (500 μL), resuspended in medium (2.5 mL), and transferred to FACS tubes. Following centrifugation at 400g for 5 minutes at 4 °C, the supernatant was discarded, and the pellet was washed with ice-cold PBS (3 mL), then centrifuged again. The pellet was resuspended in 300 μL ice-cold 50% FBS in deionised water, and cells were fixed by adding 900 μL ice-cold 70% ethanol in deionised water while vortexing. Samples were stored at 4 °C overnight. After centrifugation and washing with ice-cold PBS (3 mL), the pellet was resuspended in 500 μL ice-cold PI staining solution (50 μg mL^{-1} propidium iodide and 100 μg mL^{-1} RNase A) in PBS and incubated for 90 minutes at 37 °C, protected from light. Samples were kept on ice before flow cytometry analysis using the BD LSR Fortessa X-20 Cell Analyzer. Data was processed with BD FACSDiva 8.0.1 software.

Kinome profiling

The kinase profiling was conducted by Reaction Biology Europe GmbH. The assay format is the 33PanQinase™ assay which is based on the transfer of 33P-labelled phosphate from ATP to the kinase substrate. The compound was tested against a panel of 340 wild-type kinases. The compound was tested at a single dose of 1 μM, in duplicate, with ATP concentrations depending on apparent ATP-Km. DMSO was used as negative control.

In silico docking studies

The crystal structures of Aurora-A in complex with ADP was downloaded from the RCSB PDB website (PDB entries 1MQ4). Solvent molecules were removed. DataWarrior was used to generate optimised 3D conformations of **2D7**. The docking was performed with AutoDock,[50] and the docking side was set at the amino acids forming the ATP-binding pocket, as reported for the crystal structure. 9 poses of **2D7** were generated and the predicted affinity was calculated by AutoDock Vina, giving a binding free energy of −9.4 kcal mol^{-1}.

Data availability

In silico docking studies: the minimised energy 3D conformation of the lead compound **2D7** was generated by DataWarrior, and the optimised structure was independently

docked into the kinase domain of the protein using AutoDock Vina and visualised by PyMOL.

Conflicts of interest

The authors declare no conflicts of interest.

Acknowledgements

CCAA is grateful to the National Council of Humanities, Sciences, and Technologies (CONHACYT). YG and AUB thanks EPSRC (Horizon Europe Guarantee, EP/Y023390/1) for funding. We also thank IGC Drug Discovery Hub for financial support and Anil Rustig, University of Pennsylvania, and Ted Hupp, University of Edinburgh, for provision of EPC-2 and CP-A cells, respectively. We are thankful to the FACS facility of the IGC.

Notes and references

1 H. Sung, J. Ferlay, R. L. Siegel, M. Laversanne, I. Soerjomataram, A. Jemal and F. Bray, *Ca-Cancer J. Clin.*, 2021, **71**, 209–249.
2 M. Schweigert, A. Dubecz, H. J. Stein, M. Schweigert, A. Dubecz and H. J. Stein, *Nat. Rev. Gastroenterol. Hepatol.*, 2013, **10**, 230–244.
3 P. S. N. van Rossum, N. H. Mohammad, F. P. Vleggaar and R. van Hillegersberg, *Nat. Rev. Gastroenterol. Hepatol.*, 2018, **15**, 235–249.
4 Cancer Research UK, **https://www.cancerresearchuk.org/**, (accessed 14 April 2022).
5 National Cancer Institute, **https://www.cancer.gov/**, (accessed 14 April 2022).
6 M. Secrier, *et al.*, *Nat. Genet.*, 2016, **48**, 1131–1141.
7 T. Pradhan, O. Gupta, G. Singh and V. Monga, *Eur. J. Med. Chem.*, 2021, **221**, 113495.
8 X. Lin, X. Xiang, L. Hao, T. Wang, Y. Lai, M. Abudoureyimu, H. Zhou, B. Feng, X. Chu and R. Wang, *Am. J. Cancer Res.*, 2020, **10**, 2705.
9 K. Sasai, W. Treekitkarnmongkol, K. Kai, H. Katayama and S. Sen, *Front. Oncol.*, 2016, **6**, 247.
10 A. Tang, K. Gao, L. Chu, R. Zhang, J. Yang and J. Zheng, *Oncotarget*, 2017, **8**, 23937.
11 B. Goldenson and J. D. Crispino, *Oncogene*, 2014, **34**, 537–545.
12 D. Zheng, J. Li, H. Yan, G. Zhang, W. Li, E. Chu and N. Wei, *Acta Pharm. Sin. B*, 2023, **13**, 2826–2843.
13 K. Shi, J. Z. Zhang, L. Yang, N.-N. Li, Y. Yue, X.-H. Du, X.-Z. Zhang, Y. C. Lu and D. Guo, *BMC Cancer*, 2021, **21**, 1196.
14 Q. Chen, J. Li, X. Yang, J. Ma, F. Gong and Y. Liu, *BMC Cancer*, 2020, **20**, 372.
15 W. Zhou, S. Guo, J. Zhang, Y. Yan, J. Wu and X. Liu, *Comput. Biol. Med.*, 2024, **168**, 107759.
16 T. Tong, Y. Zhong, J. Kong, L. Dong, Y. Song, M. Fu, Z. Liu, M. Wang, L. Guo, S. Lu, M. Wu and Q. Zhan, *Clin. Cancer Res.*, 2004, **10**, 7304–7310.
17 H. Lu, *et al.*, *Cancers*, 2022, **14**, 1401.
18 V. Asati, A. Anant, P. Patel, K. Kaur and G. D. Gupta, *Eur. J. Med. Chem.*, 2021, **225**, 113781.
19 A. Dorababu, *Arch. Pharm.*, 2022, **355**, e2200154.
20 D. J. Baillache and A. Unciti-Broceta, *RSC Med. Chem.*, 2020, **11**, 1112–1135.
21 F. Carles, S. Bourg, C. Meyer and P. Bonnet, *Molecules*, 2018, **23**, 908.
22 D. S. Wishart, C. Knox, A. C. Guo, S. Shrivastava, M. Hassanali, P. Stothard, Z. Chang and J. Woolsey, *Nucleic Acids Res.*, 2006, **34**, D668–D672.
23 R. Roskoski, *Pharmacol. Res.*, 2024, **200**, 107059.
24 C. C. Ayala-Aguilera, T. Valero, Á. Lorente-Macías, D. J. Baillache, S. Croke and A. Unciti-Broceta, *J. Med. Chem.*, 2022, **65**, 1047–1131.
25 D. Hempel, T. Wieland, B. Solfrank, V. Grossmann, J. Steinhard, A. Frick, L. Hempel, T. Eberl and A. Gaumann, *Oncologist*, 2020, **25**, e881.
26 U.S. Food and Drug Administration, **https://www.fda.gov/**, (accessed 14 April 2022).
27 J. A. Ajani, K. Harada, J. E. Rogers, M. Iwatsuki, K. Yamashita and H. Baba, *F1000Research*, 2020, **9**, 1189.
28 C. Fraser, J. C. Dawson, R. Dowling, D. R. Houston, J. T. Weiss, A. F. Munro, M. Muir, L. Harrington, S. P. Webster, M. C. Frame, V. G. Brunton, E. E. Patton, N. O. Carragher and A. Unciti-Broceta, *J. Med. Chem.*, 2016, **59**, 4697–4710.
29 C. Temps, D. Lietha, E. R. Webb, X. F. Li, J. C. Dawson, M. Muir, K. G. Macleod, T. Valero, A. F. Munro, R. Contreras-Montoya, J. R. Luque-Ortega, C. Fraser, H. Beetham, C. Schoenherr, M. Lopalco, M. J. Arends, M. C. Frame, B. Z. Qian, V. G. Brunton, N. O. Carragher and A. Unciti-Broceta, *Cancer Res.*, 2021, **81**, 5438–5450.
30 C. Fraser, N. O. Carragher and A. Unciti-Broceta, *MedChemComm*, 2016, **7**, 471–477.
31 T. Valero, D. J. Baillache, C. Fraser, S. H. Myers and A. Unciti-Broceta, *Bioorg. Med. Chem.*, 2020, **28**, 115215.
32 S. H. Myers, C. Temps, D. R. Houston, V. G. Brunton and A. Unciti-Broceta, *J. Med. Chem.*, 2018, **61**, 2104–2110.
33 O. Cruz-López, C. Temps, B. Longo, S. H. Myers, F. Franco-Montalban and A. Unciti-Broceta, *ACS Omega*, 2019, **4**, 21620–21626.
34 D. J. Baillache, T. Valero, Á. Lorente-Macías, D. J. Bennett, R. J. R. Elliott, N. O. Carragher and A. Unciti-Broceta, *RSC Med. Chem.*, 2023, **14**, 2611–2624.
35 B. Apsel, J. A. Blair, B. Gonzalez, T. M. Nazif, M. E. Feldman, B. Aizenstein, R. Hoffman, R. L. Williams, K. M. Shokat and Z. A. Knight, *Nat. Chem. Biol.*, 2008, **4**, 691–699.
36 W. Zhang, D. DeRyckere, D. Hunter, J. Liu, M. A. Stashko, K. A. Minson, C. T. Cummings, M. Lee, T. G. Glaros, D. L. Newton, S. Sather, D. Zhang, D. Kireev, W. P. Janzen, H. S. Earp, D. K. Graham, S. V. Frye and X. Wang, *J. Med. Chem.*, 2014, **57**, 7031–7041.
37 C. Wang, H. Liu, Z. Song, Y. Ji, L. Xing, X. Peng, X. Wang, J. Ai, M. Geng and A. Zhang, *Bioorg. Med. Chem. Lett.*, 2017, **27**, 2544–2548.
38 S. A. Ramachandran, P. S. Jadhavar, M. P. Singh, A. Sharma, G. N. Bagle, K. P. Quinn, P.-Y. Wong, A. A. Protter, R. Rai, S. M. Pham and J. N. Lindquist, *Bioorg. Med. Chem. Lett.*, 2017, **27**, 750–754.

39 K.-D. Wu, G. S. Chen, J.-R. Liu, C.-E. Hsieh and J.-W. Chern, *ACS Med. Chem. Lett.*, 2019, **10**, 22.
40 H. R. Elgiushy, S. F. Hammad, A. S. Hassan, N. Aboutaleb and K. A. M. Abouzid, *J. Adv. Pharm. Educ. Res.*, 2018, **2**, 221–237.
41 P.-H. Su, S.-W. Hsueh, C.-K. Tseng, M.-M. Ho, P.-J. Su, C.-Y. Hung, K.-Y. Yeh, P.-H. Chang, Y.-S. Hung, Y.-W. Ho, Y.-C. Lin and W.-C. Chou, *In Vivo*, 2021, **35**, 3391–3399.
42 M. C. A. Palanca-Wessels, *et al.*, *Carcinogenesis*, 2003, **24**, 1183–1190.
43 H. Harada, H. Nakagawa, K. Oyama, M. Takaoka, C. D. Andl, B. Jacobmeier, A. von Werder, G. H. Enders, O. G. Opitz and A. K. Rustgi, *Mol. Cancer Res.*, 2003, **1**, 729–738.
44 K. S. Metz, *Cell Syst.*, 2018, **7**, 247–350.
45 A. Essakly, H. Loeser, M. Kraemer, H. Alakus, S. H. Chon, T. Zander, R. Buettner, A. M. Hillmer, C. J. Bruns, W. Schroeder, F. Gebauer and A. Quaas, *Transl. Oncol.*, 2020, **13**, 157.
46 L. Wang, L. Shan, S. Zhang, J. Ying, L. Xue, Y. Yuan, Y. Xie and N. Lu, *PLoS One*, 2014, **9**, e103021.
47 F. Janku, T. A. Yap and F. Meric-Bernstam, *Nat. Rev. Clin. Oncol.*, 2018, **15**, 273–291.
48 T. Machleidt, C. C. Woodroofe, M. K. Schwinn, J. M. M. B. Robers, K. Zimmerman, P. Otto, D. L. Daniels, T. A. Kirkland and K. V. Wood, *ACS Chem. Biol.*, 2015, **10**, 1797–1804.
49 J. Nowakowski, C. N. Cronin, D. E. McRee, M. W. Knuth, C. G. Nelson, N. P. Pavletich, J. Rogers, B. C. Sang, D. N. Scheibe, R. V. Swanson and D. A. Thompson, *Structure*, 2002, **10**, 1659–1667.
50 T. Sander, J. Freyss, M. von Korff and C. Rufener, *J. Chem. Inf. Model.*, 2015, **55**, 460–473.
51 O. Trott and A. J. Olson, *J. Comput. Chem.*, 2010, **31**, 455–461.
52 L. Schrödinger and W. DeLano, *PyMOL*, 2020, **http://www.pymol.org/pymol**.